Erosion of neutron-producing targets at ISIS Spallation Neutron Source

G J Burns, A Dey, D J S Findlay, D J Haynes, D M Jenkins, L G Jones, J D Moor and G P Škoro

Published version information

Citation: G Burns et al. 'Erosion of neutron-producing targets at ISIS spallation neutron source.' Nucl Instrum Meth B 521 (2022): 7-16.

DOI: 10.1016/j.nimb.2022.04.004

Erosion of neutron-producing targets at ISIS Spallation Neutron Source

G J Burns, A Dey, D J S Findlay, D J Haynes, D M Jenkins, L G Jones,
J D Moor and G P Škoro
ISIS, Rutherford Appleton Laboratory, Chilton, Oxon OX11 0QH, UK

Abstract

Rates of erosion of neutron-producing targets at the ISIS Spallation Neutron and Muon Source are deduced on the basis of gamma-ray spectrometry. The results suggest that for TS-1 targets erosion rates decrease with time, whereas erosion rates for TS-2 targets increase with time. Absolute masses eroded over typical target lifetimes are several milligrams of tantalum for TS-1 targets, and ~1 gram of tungsten for TS-2 targets.

1. Introduction

In order to promote research into the structure and dynamics of molecular matter, several spallation neutron sources are in operation around the world. In such sources the proton beam from a high-power particle accelerator is directed on to a high-atomic-number target, and neutrons are produced from the target by spallation [1]. These neutrons are then moderated to thermal and epithermal energies to enable samples of molecular matter to be investigated using elastic and inelastic neutron scattering techniques. Proton beam powers from the accelerators typically lie in the range ~100 kW – 2 MW, so much heat is dissipated in the target, and the target becomes highly radioactive. Consequently, in the interests of both operational and financial efficiency, the longevity of such targets is important.

Spallation neutron targets can be made of liquid metal (mercury, as at SNS [2] and J-PARC [3]), water-cooled zircaloy-clad lead (as at PSI [4]), and water-cooled tantalum-clad tungsten (as at CSNS [5], ISIS [6] and LANSCE [7]), and a helium-cooled rotating tungsten target is being built at ESS [8]. Information on the operational characteristics of these different designs of targets is available, for example through the long-running International Collaboration on Advanced Neutron Sources [9] (established in 1977). In the interests of maximising the efficiency of cold-neutron production, the Second Target Station (TS-2) [10] at ISIS uses a compact tantalum-clad solid tungsten target of novel design, but some difficulties over degradation of the tantalum cladding have been encountered [11].

In a previous publication [12] on erosion in ISIS TS-2 targets, only time dependences of erosion were presented, but in the present paper analyses with an improved model giving estimates of absolute masses of material eroded are presented — both for ISIS TS-1 targets and for ISIS TS-2 targets.

The obvious way to investigate erosion in irradiated targets is to make use of a post-irradiation examination (PIE) facility. However, so far at ISIS, a heavily committed user-based operational facility, resources to set up such a facility have not been available. Neither have resources been available to carry out the work at a hired facility.

Consequently, *faute de mieux*, methods based on gamma-ray spectrometry have been developed to measure the consequences of erosion, and it is with this gamma-ray-based 'proxy' method that the present paper is concerned. Of course, it is realised that this proxy method is not ideal, but, from an operational point of view, progress on assessing target performance must nonetheless be made, and the results of the proxy method can be expected to guide both future work on target design and future work in a PIE facility.

2. ISIS neutron-producing targets

The ISIS Spallation Neutron and Muon Source [6, 10] is driven by an 800-MeV ~250-μA proton synchrotron running at 50 pulses per second (pps). The proton beam from the synchrotron is split and delivered at 40 pps to Target Station 1 (TS-1) and at 10 pps to Target Station 2 (TS-2). Conditions experienced by ISIS neutron-producing targets are listed in Table 1, and diagrams of the targets, including dimensions, are shown in Figs. 1 and 2. It is evident that, especially at the front of the target, a TS-2 target is more highly stressed than a TS-1 target. Table 2 lists the operational history of tantalum-clad tungsten targets at ISIS.

Over the past two decades, TS-1 targets have been replaced only because one or two of the thermocouples incorporated in the target plates have failed, never because any material damage has occurred to the structure of the target itself. However, several TS-2 targets have had to be replaced because activity leaking into the cooling water circuits from breaches of the tantalum cladding began to make routine operational work in the target services area difficult because of increasing radiation dose rates.

Target type	Coolant	Proton energy on target, MeV	Proton current on target, μA	Rep. rate, s^{-1}	$1/e$ beam radius r_b on target, cm	Energy per ~0.5 μs pulse, kJ	Nominal heat load per pulse, kJ cm^{-2}
TS-1	D_2O	800	200	40	2.53	4.0	0.2
TS-2	H_2O	800	40	10	0.85	3.2	1.4

Table 1. Conditions experienced by ISIS neutron-producing targets. The radial profiles of the beam spots on target are *approximately* [13] gaussian, *i.e.* the beam current density j (μA cm^{-2}) is $j(r) \cong (I/(\pi r_b^2)) \exp(-r^2/r_b^2)$ where I is the proton beam current (μA) and r_b (cm) is both the $1/e$ radius and the root-mean-square radius. The TS-1 target coolant is actually a mixture of ~80% D_2O and ~20% H_2O.

TS-1 target no.	Irradiated	milliamp-hours
W#1	May 2001 – Jul. 2005	2660
W#2	Sep. 2005 – Mar. 2009	1950
W#3	May 2009 – Aug. 2014	2900
W#4	Mar. 2015 – Jun. 2021	3700
TS-2 target no.	Irradiated	milliamp-hours
#1	Sep. 2008 – Dec. 2009	115
#2	Feb. 2010 – May 2010	36
#3	Mar. 2011 – Nov. 2012	212
#4	Nov. 2012 – Jun. 2014	230
#6	Jul. 2014 – Jul. 2015	103
#7	Sep. 2015 – Jun. 2017	280
#8	Sep. 2017 – Mar. 2019	232
#9	Jun. 2019 – Jun. 2021	253

Table 2. Irradiation times of TS-1 and TS-2 targets on ISIS, and integrated proton beam currents delivered to targets during ~30–50-day-long irradiation campaigns ('user runs'). (TS-2 target #5 was never installed.) Some ~1–2% extra integrated beam current is usually delivered to target before each irradiation campaign while setting up.

When a target is replaced, the cooling water is filtered, filters are renewed, and the ion-exchange columns that control water chemistry are replaced by fresh ion-exchange columns; consequently, activity in and around these items of ancillary plant and equipment is significantly reduced. But, because some activity inevitably remains lodged in pumps, valves, pipe bends, *etc.*, non-negligible amounts of activity remain.

3. Gamma-ray spectrometry in target service areas

Associated with each of the TS-1 and TS-2 target stations is a target services area, TSA1 for TS-1, and TSA2 for TS-2. In each target services area are located the pumps, heat exchangers, filters, ion-exchange columns, *etc.* involved in circulating cooling water through the target, and this equipment, together with room-temperature and cryogenic plant for the neutron moderators, is all carried on a movable target services platform (see Fig. 3). The essential assumption underlying the present paper is that activity eroded from a target ends up in the target services area platform (in filters, ion-exchange columns, pumps, *etc.*) where it can be seen by an HPGe gamma-ray detector. From the position on the target services platform of the filters, ion-exchange columns, pumps, *etc.* in which material eroded from the target would be accumulated, active material eroded from the target was assumed to be concentrated at a position 1.0 ± 0.3 m forward of the back edge of the platform.

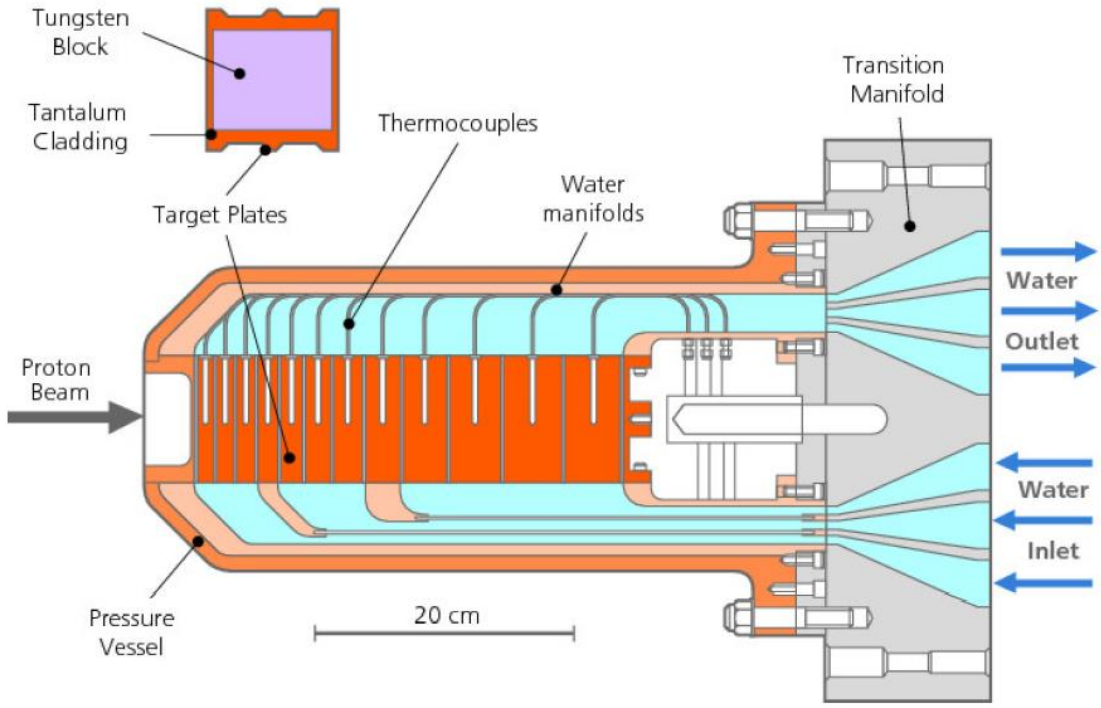

Fig. 1. ISIS TS-1 target (plan view). The twelve tungsten plates, 105 × 80 mm in area, range from 11 to 46 mm in thickness, and are clad by 2.00 mm and 1.75 mm tantalum on the large-area and small-area surfaces respectively. Water (~80% D_2O, ~20% H_2O) circulates through the gaps between the plates at a total rate of ~500 litres min^{-1}, corresponding to a water flow speed of ~3–4 m s^{-1}.

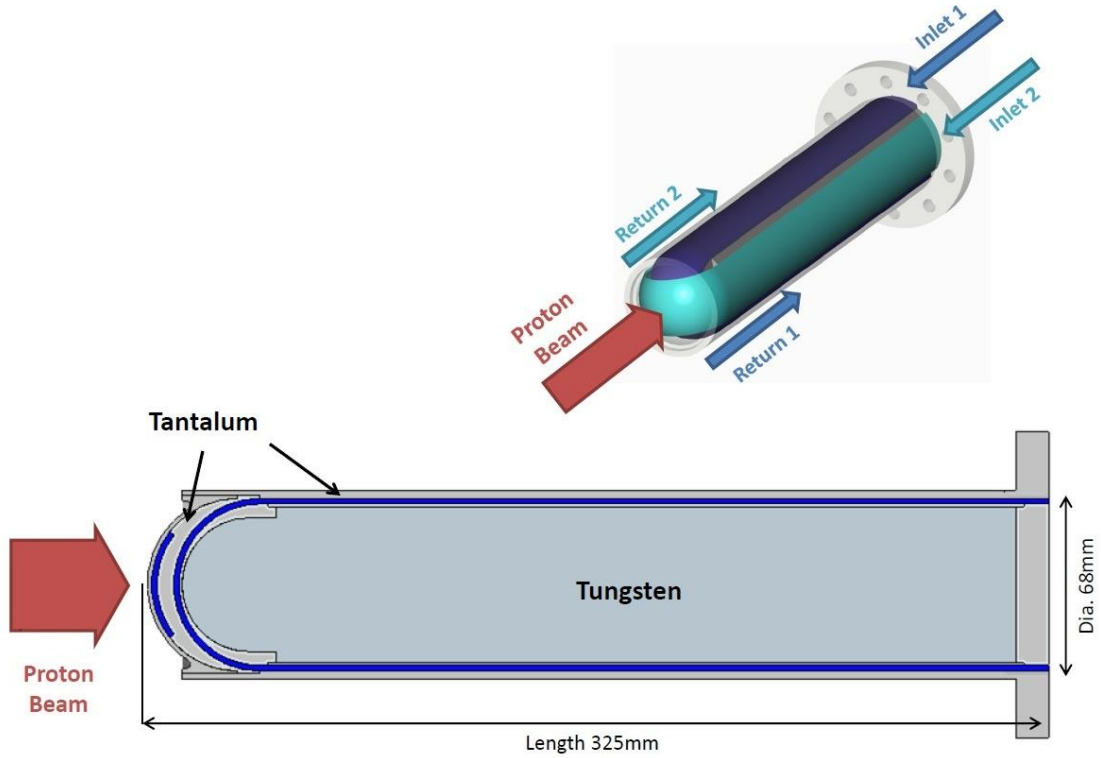

Fig. 2. ISIS TS-2 target. Tantalum cladding thickness over tungsten core, 0.9 mm; thickness of tantalum outer casing, 2.3 mm; thickness of water channel between cladding and casing, 2.0 mm. Along axis from front of target: 1.5 mm Ta, 2.0 mm water, 6.0 mm Ta, 2.0 mm water, 1.0 mm Ta. Water (H_2O) circulates through each flow-and-return circuit at a rate of ~45 litres min^{-1}, corresponding to a water flow speed of ~10 m s^{-1}.

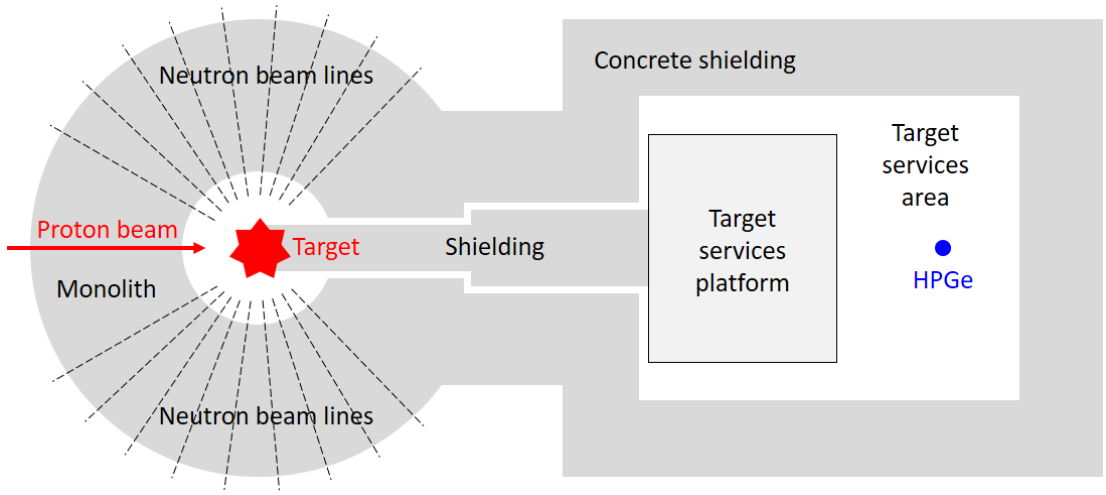

Fig. 3. Generalised *schematic* diagram of neutron-producing target, monolith and target services area for both TS-1 and TS-2 target stations. Not to scale! The monolith is several thousands of tons of steel and concrete shielding surrounding the neutron-producing target.

In the target services area TSA1 for the TS-1 target station, gamma-ray spectrometry measurements were made in the years 2016, 2017, 2018, 2019 and 2021[1] following the ends of ~30–50-day-long irradiation campaigns. The gamma-ray spectrometry measurements were made using an electro-mechanically cooled Canberra Falcon 5000 high-purity germanium (HPGe) gamma-ray spectrometer with a BE2830 germanium crystal, and the HPGe detector was always positioned in the same place in TSA1, 5.5 m behind the back edge of the target services platform (so that the overall active-material-to-detector distance was 6.5 ± 0.3 m). For all years except 2021, several or many successive gamma-ray spectra were measured, immediately following each other, but for all years measurement of spectra began at times between 60 and 75 hours after the end of full-power running to target, and dead times all lay within the range 6.2–7.5%. A typical spectrum is shown as Fig. 4.

In the target services area TSA2 for the TS-2 target station, the gamma-ray spectrometry measurements were made using the same HPGe detector, again always positioned in the same place in TSA2, and again 5.5 m behind the back edge of the target services platform, and the measurements were made both during 1-day maintenance shutdowns during ~30–50-day-long irradiation campaigns and at the ends of the campaigns. Sixty-six measurements were made between the years 2013 and 2021 inclusive. Spectra were usually recorded over a real time of 4 hours beginning some 2½ hours after beam-off. Dead times were usually ~20%. A typical spectrum is shown as Fig. 5.

[1] There was no measurement in 2020, essentially due to restrictions imposed because of the coronavirus disease (COVID-19) pandemic.

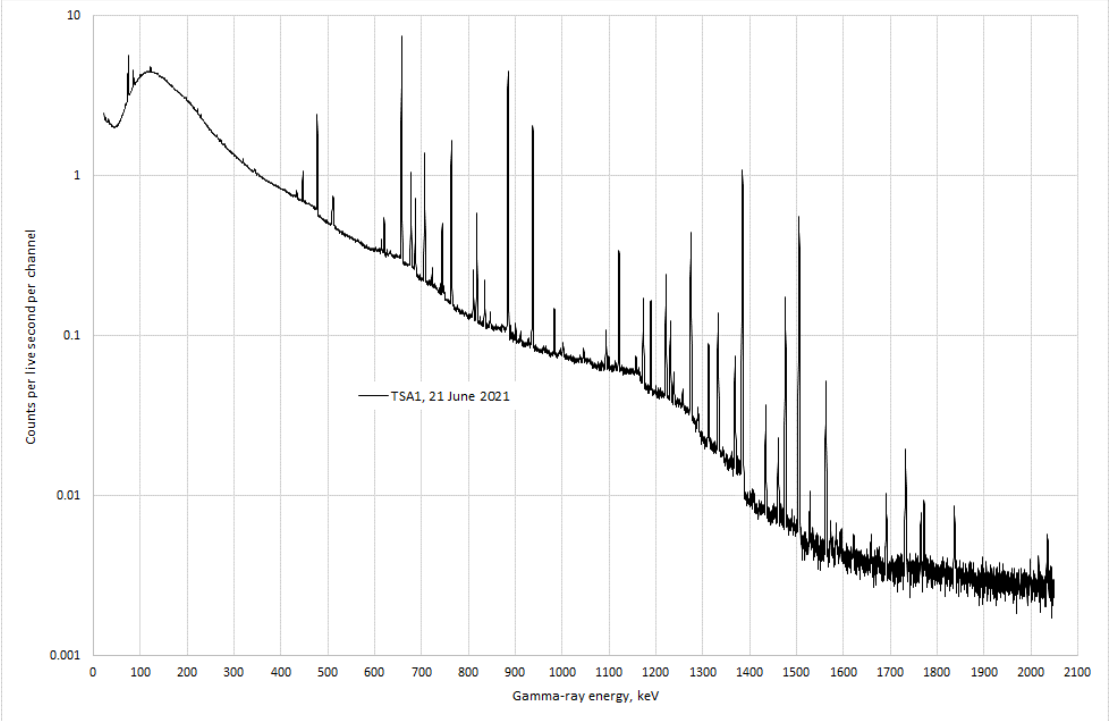

Fig. 4. Typical gamma-ray spectrum in target services area TSA1 for target station TS-1. The prominent lines are mostly from ^{110m}Ag (from erosion of silver seals used in the target cooling water circuit) and ^{182}Ta (from erosion of tantalum cladding).

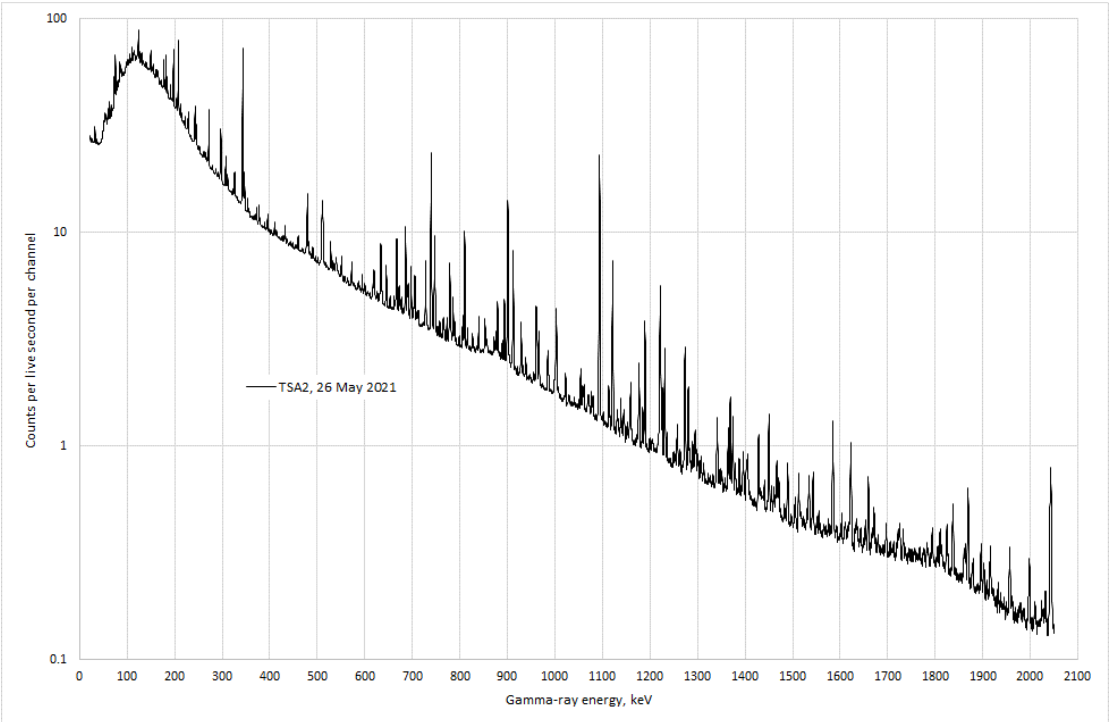

Fig. 5. Typical gamma-ray spectrum in target services area TSA2 for target station TS-2. It is clear that there are many more radionuclide lines visible than there are in Fig. 4. The most prominent lines are from ^{170}Lu, ^{171}Lu, ^{172}Lu, ^{175}Hf and ^{182}Ta (all from erosion of exposed tungsten, although for ^{182}Ta a small contribution may be present from erosion of the tantalum cladding).

4. Modelling erosion

The model being assumed in the present paper is that radioactive material eroded from a target accumulates in the target services area where it is visible to the gamma-ray spectrometer during maintenance days in the middle of irradiation campaigns and at the ends of campaigns. This model improves upon the model described in [12]

If it be assumed that the number of atoms of a given radionuclide in the target is $N_t = N_t(t)$ where t is time, then the equation describing build-up of activity of the radionuclide in the target is

$$dN_t = r\, I(t)\, dt \; - \; \lambda N_t\, dt \qquad \text{eq. 1}$$

where $I = I(t)$ is the proton beam current, $\lambda = \ln(2)/t_{1/2}$, $t_{1/2}$ is the half-life of the radionuclide, and r is the production rate of radionuclide atoms per unit beam current and per unit time. If it be further assumed that the number of atoms of the same radionuclide accumulating in the target services area is $N_s = N_s(t)$, then

$$dN_s = s(t)\, N_t\, dt - \lambda N_s\, dt \qquad \text{eq. 2}$$

where $s = s(t)$ is the rate at which radionuclide atoms are eroded from the target. If some suitable form is assumed for $s = s(t)$, then, since $I = I(t)$ is a known function of time, these two differential equations can be integrated to give activity $\lambda N_s = \lambda N_s(t)$ which can be assumed to be proportional to the count rate from the radionuclide measured in the target services area.

The first step in computing $N_s = N_s(t)$ is to integrate eq. 1 taking $I = I(t)$ from the actual pattern of irradiation campaigns and setting N_t to zero whenever a spent target is removed and a fresh target is installed. The second step in computing $N_s = N_s(t)$ is to integrate eq. 2 using $N_t = N_t(t)$ from eq. 1 and to allow N_s to take on values to be determined from fitting the measured count rate data whenever a spent target is removed and a fresh target is installed — as was stated in Sect. 2, when a target is replaced, activity in the target services area is reduced, but not reduced to zero, and not by a predictable amount.

To obtain absolute erosion rates using this model, it is necessary to know at some point in time the absolute activity of radionuclides in the target services areas so that the constants of proportionality between count rates and activities may be established. Of course, in principle, such absolute activities could be obtained by dismantling the equipment in the target services area and making detailed measurements on the many resultant items of plant and equipment, but, needless to say, it is completely unrealistic to think that in practice such a course of action could be followed in a heavily committed operational facility like ISIS. It is therefore necessary to fall back on the technique of using observed count rates from radionuclides emitting several or many gamma-ray lines to estimate thicknesses of attenuating media and consequently deducing absolute activities therefrom [14, 15]. It is recognised, of course, that such a procedure can result in underestimates, as it is possible that activity is lodged in places which the HPGe detector simply cannot see. But the filters, ion-exchange columns, pumps, *etc.*, items in which activity is likely to be lodged, are visible to the HPGe detector, and so it is likely that the degree of underestimation is small.

5. Erosion in TS-1 targets

Since gamma-ray spectrometry in the target services area TSA1 for TS-1 was begun only in 2016, estimates of erosion can be obtained only for TS-1 target W#4.

5.1 Absolute erosion rate

Assuming that for TS-1 targets the relevant radionuclide to consider is ^{182}Ta, Fig. 6 shows the count rate for the 1121-keV ^{182}Ta line as a function of time. On the face of it, the graph suggests that erosion of the tantalum cladding of the target is gradually decreasing with time, but it should be noted that, because of reasons associated with the coronavirus disease (COVID-19) pandemic, ISIS did not run for many months during the year 2020, and so the 2021 datum may be anomalously low.

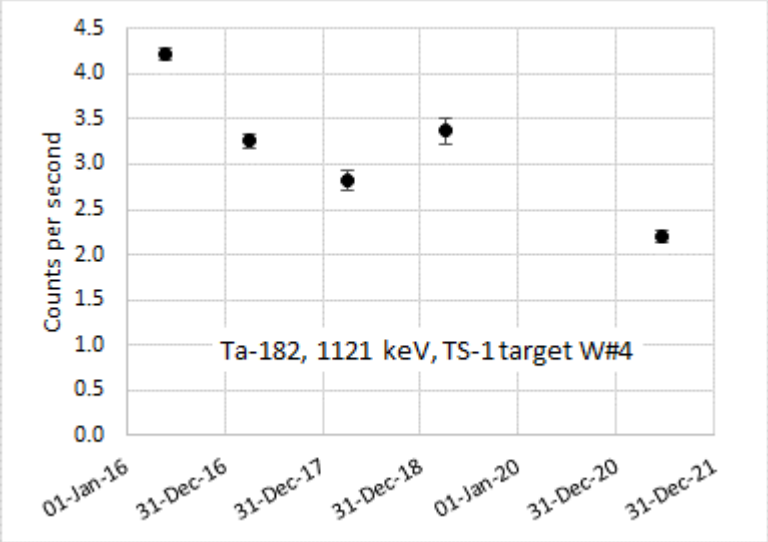

Fig. 6. Count rates from the HPGe gamma-ray detector for the 1121-keV line from ^{182}Ta as a function of time for TS-1 target W#4. The number of contiguously successive gamma-ray spectra measured in 2016, 2017, 2018, 2019 and 2021 were 11, 8, 18, 23 and 1 respectively (a total of 61 spectra).

The method outlined in Sect. 4 was used to obtain an absolute value for ^{182}Ta activity in the target services area TSA1 for TS-1 — *viz* using ratios of the decay gamma-ray lines from ^{182}Ta to estimate thicknesses of gamma-ray-attenuating media between the source of gamma-rays and the HPGe gamma-ray detector and thereby, from the known energy dependences of the mass attenuation coefficients for the attenuating media and the known energy dependence of the full-energy-peak detection efficiency of the HPGe detector, obtaining the absolute activity of ^{182}Ta behind the attenuating media. In order to increase the likelihood of making a good estimate of the absolute activity of ^{182}Ta in TSA1, it was assumed, on the basis of Fig. 6, that the absolute activity of ^{182}Ta in TSA1 was essentially constant, *i.e.* that λN_s had effectively reached saturation, so that all measured gamma-ray spectra, a total of sixty-one spectra, could be analysed together in order to improve the statistical accuracy of the result.

Although for the target services area TSA2 for TS-2, as will be seen in Sect. 6, the best fit to the data was obtained with two sources of radioactivity, one behind a low-atomic-number (low-Z) attenuating medium and the other behind a high-Z attenuating

medium, such might not necessarily have been the case for TSA1. Table 3 shows the results of fits to the gamma-ray spectra spanning 2016–2021 assuming the ^{182}Ta activity to lie behind one attenuating medium, taken in turn to be water, aluminium, iron and lead. The fits to twelve gamma-ray lines from ^{182}Ta were achieved by minimising the function $\chi^2_{\text{pdf}} = \{\sum_i (C_i - c_i)^2 / \delta C_i{}^2\}/(n-2)$ where C_i is the measured count rate for gamma-ray line i, $c_i = c(k_i) = \varepsilon(k_i)\, \alpha(k_i) \exp(-\mu/\rho(k_i)\, \rho t)\, a$, k_i is the energy of gamma-ray i, $\varepsilon(k_i)$ is the full-energy-peak efficiency [16] of the HPGe detector at energy k_i for a source-to-detector distance of 6.5 m, $\alpha(k_i)$ is the emission probability (or abundance) of gamma-ray i, $\mu/\rho(k_i)$ (cm^2 g^{-1}) is the mass attenuation coefficient [17] for the attenuating medium at energy k_i, ρt (g cm^{-2}) is the thickness of the attenuating medium, a is activity, n is the number of gamma-ray lines fitted, δC_i is the uncertainty in C_i, and the two parameters varied during the minimisation are ρt and a. However, Table 3 also shows the results of fits to the gamma-ray spectra assuming ^{182}Ta activity to be split between two separate sources behind two attenuating media, when $c_i = \varepsilon(k_i)\, \alpha(k_i)\, a\, \{f \exp(-\mu/\rho_1(k_i)\, \rho t_1) + (1-f) \exp(-\mu/\rho_2(k_i)\, \rho t_2)\}$ and the four parameters varied during minimisation are ρt_1, ρt_2, f and a. On the basis of the measures of goodness of fit χ^2_{pdf} listed in the table, the ^{182}Ta in TSA1 is taken to be 0.085 ± 0.055 GBq (where the uncertainty is the standard deviation of the sixty-one values of absolute activity extracted from the fitting process).

Attenuating medium (media)	GBq, ^{182}Ta	Thickness(es), g cm^{-2}		χ^2_{pdf}
Water	0.094 ± 0.018	23.4 ± 1.4		15.31
Al	0.075 ± 0.014	23.0 ± 1.3		7.03
Fe	0.039 ± 0.006	12.4 ± 1.2		6.32
Pb	0.034 ± 0.029	5.9 ± 9.3		34.28
Water Pb	0.085 ± 0.055	26.0 ± 7.6	0.8 ± 0.4	1.51

Table 3. Results of fits to sixty-one measured gamma-ray spectra spanning 2016–2021. The uncertainties given are the standard deviations corresponding to the sixty-one sets of activity and thickness, and the χ^2_{pdf}'s are the averages for the sets of sixty-one fits.

A value for the ^{182}Ta production rate r in a TS-1 target was obtained from Monte Carlo calculations of activity in a TS-1 target at 1 May 2019, when the ^{182}Ta activity was 1.63E+11 Bq. Activity calculations were carried out using the Monte Carlo codes MCNPX 2.70, HTAPE3X and CINDER-90 [18, 19]. Assuming that this activity λN_t can be written as $\lambda N_t = r \sum_j I_j\, (1 - \exp(-\lambda\, t_j^{\text{irr}}))\, \exp(-\lambda\, t_j^{\text{cool}})$ where $\lambda = \ln(2)/t_{1/2}$, $t_{1/2}$ is the ^{182}Ta half-life, I_j is the average beam current during irradiation campaign j, t_j^{irr} is the duration of campaign j and t_j^{cool} is the elapsed time after the end of campaign j, the value is r = 5.52E+13 μA^{-1} s^{-1}. From operational records, the overall average beam current delivered to TS-1 target W#4 during irradiation campaigns (taking into account machine trips and other beam-off times within irradiation campaigns) is 145 μA. By integrating the differential equations eqs. 1 and 2 numerically assuming r and s to be constant, and, in the currently prevailing spirit of approximation, assuming five irradiation campaigns per year each 36.5 days long (which is a good representation of the actual schedule of irradiation campaigns), and taking λN_s at saturation to be 8.5 ± 5.5 E+07 Bq as above,

$s = 2.27 \pm 1.48$ E-10 per day, or 4.14 ± 2.70 E-08 per year (assuming erosion occurs only during beam-on days).

The total tantalum mass in TS-1 targets such as target W#4 is $m_{\mathrm{tot}} = 29$ kg, and assuming the ^{182}Ta activity to be uniformly distributed throughout the tantalum, the absolute rate of tantalum erosion in TS-1 target W#4 is therefore $s\, m_{\mathrm{tot}} = 1.2 \pm 0.8$ milligrams per 180-day beam-on year. Consequently, over the several-years-long lifetime of a TS-1 target, it is likely that several milligrams of tantalum are eroded.

5.2 Time dependence of erosion

Gamma-ray spectra recorded in the target services area TSA1 for TS-1 were analysed to extract count rates for the fourteen radionuclides listed in Table 4. The radionuclides ^{46}Sc – ^{60}Co are presumed to be due to erosion of the stainless-steel pressure vessel surrounding the tantalum-clad tungsten target core, and, as already stated, ^{182}Ta is presumed to be due to erosion of the tantalum cladding around the tungsten plates in the target core ($^{110\mathrm{m}}$Ag is almost certainly due to erosion of the silver seals used in the target cooling water circuit). The radionuclides ^{7}Be, ^{22}Na and ^{24}Na are not considered further; ^{7}Be is most likely to be produced by spallation of the oxygen nuclei in the target cooling water and is therefore unlikely to be associated with erosion of the target materials; ^{22}Na is probably too far in terms of atomic number from stainless steel to be necessarily closely associated with stainless steel; and ^{24}Na has too short a half-life to be useful for the present purposes. The count rates corresponding to the gamma-ray lines were obtained automatically by locating the position of each peak i_p ($i =$ channel number) from the smoothed second derivative of the spectrum, establishing the lower and upper limits of the peak as channels i_l and i_u where $n_{i_l} - n_{i_l-1} < (n_{i_l} + n_{i_l-1})^{1/2}$ and $n_{i_u+1} - n_{i_u} < (n_{i_u} + n_{i_u+1})^{1/2}$ where n_i is the contents of channel i (*i.e.* when the base of the peak disappears into statistical insignificance), assuming the background is a straight line between channels $i_l - 1$ and $i_u + 1$, summing the background-subtracted contents of the channels between i_l and i_u inclusive, and dividing by the live time. For each peak the uncertainty in the count rate was estimated by repeatedly (one hundred times) perturbing the n_i by amounts chosen randomly from a gaussian distribution with a standard deviation ${n_i}^{1/2}$, and then taking the standard deviation of the resultant set of 'perturbed' count rates.

Erosion rates were estimated by numerically integrating the two differential equations eqs. 1 and 2 and fitting λN_s to the measured count rates to obtain the time dependence of $s = s(t)$. Values used for the proton beam current I were the average values during each irradiation campaign. To take into account likely small changes in the physical distributions of radionuclides within the hardware in TSA1 from year to year, an uncertainty of ±10% was assigned to each count rate if its statistical uncertainty was less than ±10%. Two prescriptions for $s = s(t)$ were tried: a constant rate, and a rate proportional to $\exp(a_2 t)$. Erosion was assumed to take place only when the target was being irradiated (*i.e.* $s(t) = 0$ when $I(t) = 0$), as at other times the target cooling water does not circulate through the target. Uncertainties in the parameter a_2 were obtained by perturbing the count rates by amounts chosen randomly from gaussian distributions with standard deviations equal to the uncertainties in the count rates, and then taking the standard deviation of the resultant set of 'perturbed' a_2's. Results are listed in Table 5, and a typical fit is shown in Fig. 7.

	$t_{1/2}$, days	γ-ray lines used, keV
Be-7	53.4	477.6
Na-22	950	1274.5
Na-24	0.623	1732.0 (DE)
Sc-46	83.8	889.3
V-48	16.0	983.5, 1312.1
Cr-51	27.7	320.1
Mn-54	312	834.8
Fe-59	44.6	1099.2
Co-56	77.3	846.8, 1238.3, 1771.4
Co-57	270	122.1
Co-58	70.8	810.8
Co-60	1926	1173.2, 1332.5
Ag-110m	250	446.8, 657.8, 1384.3
Ta-182	115	222.1, 1121.3

Table 4. Radionuclides, half-lives, and gamma-ray lines the count rates for which were used for extracting time dependences of erosion ('DE' = double escape).

	Erosion rate constant	Erosion rate $\propto \exp(a_2 t)$	
	χ^2_{pdf}	χ^2_{pdf}	a_2, per day
Sc-46	2.86	4.15	–0.0003 ± 0.0013
V-48	1.75	1.68	–0.0002 ± 0.0002
Cr-51	1.17	0.01	–0.0010 ± 0.0006
Mn-54	5.61	8.39	+0.0001 ± 0.0013
Fe-59	1.48	0.00	+0.0013 ± 0.0006
Co-56	3.34	1.68	–0.0009 ± 0.0003
Co-57	4.85	4.68	–0.0007 ± 0.0006
Co-58	7.98	1.82	–0.0010 ± 0.0003
Co-60	14.5	14.8	+0.0038 ± 0.0057
All nine	5.39	4.75	–0.0006 ± 0.0003
Ag-110m	8.19	9.15	–0.0002 ± 0.0010
Ta-182	1.78	1.79	–0.0003 ± 0.0003

Table 5. Results of fits to measured count rate data for TS-1 target W#4 assuming a constant erosion rate and an erosion rate varying exponentially with 'beam-on' time. For the constant-erosion-rate fits two parameters were fitted, the earliest count rate and the erosion rate; for the time-dependent-erosion-rate fits three parameters were fitted, the earliest count rate, and a_1 and a_2 in the erosion rate equation $a_1 \exp(a_2 t)$. Since there are only five data points, for the same deviation of the fitted curve from the data points, the goodness-of-fit parameter χ^2_{pdf} for the time-dependent fit is necessarily greater by a factor 3/2 than it is for the constant fit, which explains, for example, why for ^{54}Mn the χ^2_{pdf} for the time-dependent fit appears worse than it is for the constant fit. Uncertainties quoted are in accordance with 'external consistency', *i.e.* they have been multiplied by $\chi^{2\ 1/2}_{\text{pdf}}$ when $\chi^2_{\text{pdf}} > 1$.

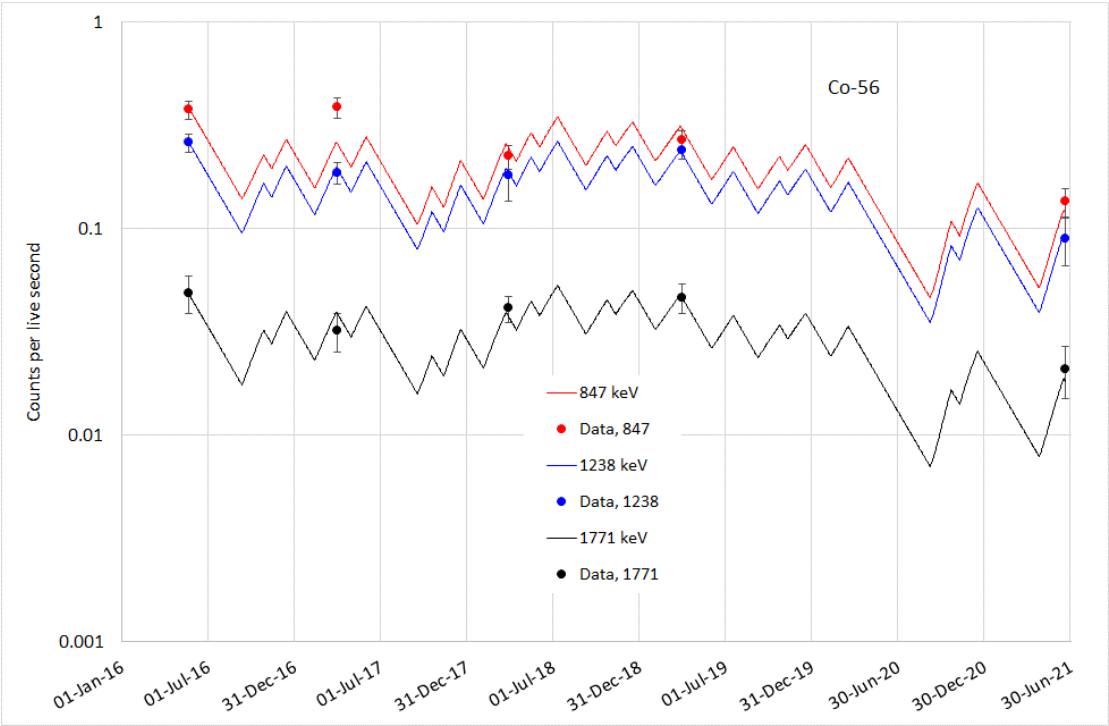

Fig. 7. Fits to ^{56}Co count rate data, TS-1 W#4 target. The rising parts of the lines correspond to beam-on periods, and the falling parts to beam-off periods.

With measurements available at only five points in time during the ~6-year operational lifetime of the TS-1 W#4 target, good precision in describing the time dependence of erosion can hardly be expected. Nevertheless, from Table 5, indications are that on the whole erosion rates do decrease with time. (This, as will be seen in Sect. 6 below, is in contrast with results of analyses of several tens of gamma-ray spectra spread over several years which show that erosion in TS-2 targets increases with time — although, of course, such an increasing rate of erosion is almost certainly due to breach(es) of the tantalum cladding around TS-2 target tungsten cores.)

There are two obvious outliers in Table 5, ^{59}Fe and ^{60}Co, and fits for both of these are shown in Fig. 8. For ^{59}Fe, there would appear to be nothing amiss with the fit; in fact, presumably by chance, the fit is remarkably good. For ^{60}Co, count rates for April 2017 appear to be anomalously high, but the most likely reason would have been the unsuspected presence of ^{60}Co-bearing material near the HPGe detector, since, after all, ^{60}Co is widespread throughout the neutron-generating ISIS facility. However, for all nine radionuclides ^{46}Sc – ^{60}Co fitted simultaneously, $a_2 = -0.0006 \pm 0.0003$ per day, and so an erosion rate decreasing with time is reasonably clear.

It is not impossible to imagine that an erosion rate decreasing with time is consistent with initial surface roughness being smoothed as erosion proceeds, and that the rate of decrease for tantalum is smaller than the rate of decrease for stainless steel because resistance to corrosion is known to be greater for tantalum than for stainless steel [20, 21, 22] (although in none of these three references was the physical and chemical environment in which the measurements were made identical to that which prevails inside a spallation neutron target during irradiation).

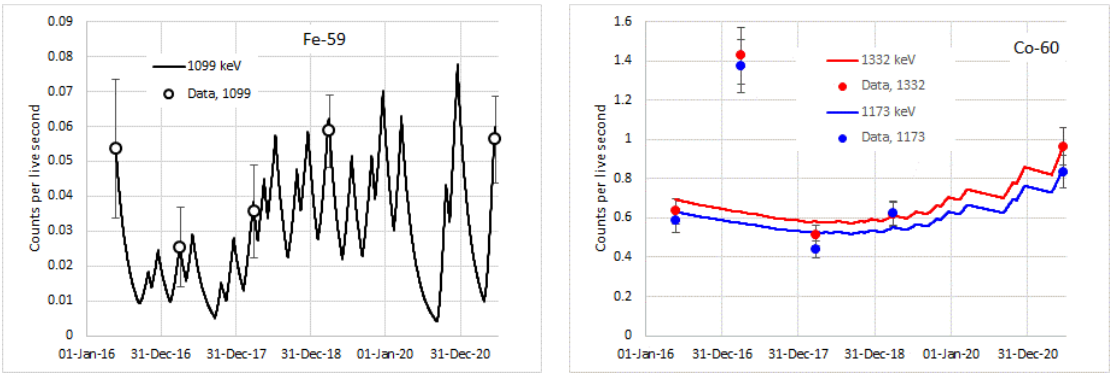

Fig. 8. Fits to ^{59}Fe and ^{60}Co count rate data. Otherwise same as Fig. 7.

6. Erosion in TS-2 targets

As is evident from Fig. 5, signatures of many radionuclides are seen in the target services area TSA2 for TS-2, such radionuclides including ^{167}Tm, ^{169}Yb, ^{172}Lu, ^{172}Hf, ^{175}Hf, ^{182}Ta, ^{183}Re and ^{184}Re and/or ^{184m}Re — three of which, ^{183}Re, ^{184}Re and ^{184m}Re, can arise only from the tungsten core of the target and not from the tantalum cladding around the core. Estimates of absolute activities of these radionuclides were made in the same way as described in Sect. 5, *viz* using ratios of decay gamma-ray lines to estimate thicknesses of gamma-ray-attenuating media between sources of gamma-rays and the HPGe gamma-ray detector and thereby, from the known energy dependences of the mass attenuation coefficients for the attenuating media and the known energy dependence of the full-energy-peak detection efficiency of the HPGe detector, obtaining absolute activities.

6.1 Absolute activities

Count rates were taken from a 40-hour-long gamma-ray spectrum measured in TSA2 during 19–21 December 2020. Seventeen prominent gamma-ray lines spanning the range 110–1915 keV were used to establish a correction to the nominal energy calibration of the spectrometer good to ±0.03 keV, and also to establish the dependence of peak full width at half maximum (FWHM) as a function of gamma-ray energy good to better than ±0.1 keV. Based on the energy scale and FWHMs established thereby, strengths of gamma-ray lines in terms of counts per second were obtained for several radionuclides. Contributions by ^{183}Re and ^{183}Ta to the same decay gamma-ray lines (both ^{183}Re and ^{183}Ta decay to ^{183}W) were separated on the basis of differences in gamma-ray emission probabilities, and a similar separation was made for ^{184}Re and ^{184}Ta. Contributions by ^{184}Re and ^{184m}Re could not be separated in this way, since the one line at 104.7 keV unique to ^{184m}Re was not visible, and so ^{184m}Re was not considered further. Uncertainties in count rates were obtained using the perturbation method described above. Results are listed in Table 6.

Radionuclide	Line used	χ^2_{pdf}	Activity, GBq	Attenuation thickness, g cm^{-2}	
				Water	Pb
^{167}Tm	208 keV	5.06	1.78 ± 0.49	11.4 ± 1.4	50 ± 15
^{169}Yb	177 keV	5.06	2.16 ± 0.66	11.4 ± 1.4	50 ± 15
^{172}Lu	(31 lines)	10.9	2.59 ± 0.37	15.7 ± 1.0	65 ± 33
^{172}Hf	126 keV	5.06	0.89 ± 0.30	11.4 ± 1.4	50 ± 15
^{175}Hf	343 keV	5.06	2.07 ± 0.55	11.4 ± 1.4	50 ± 15
^{182}Ta	(10 lines)	10.9	2.03 ± 0.31	15.7 ± 1.0	65 ± 33
^{183}Re	162 keV	5.06	0.012 ± 0.016	11.4 ± 1.4	50 ± 15
^{184}Re	903 keV	5.06	0.042 ± 0.006	11.4 ± 1.4	50 ± 15

Table 6. Activities for eight radionuclides at 19–21 December 2020 (split behind water and lead attenuating media as in Sect. 5.1). The activities and attenuation thicknesses for the six radionuclides ^{167}Tm, ^{169}Yb, ^{172}Hf, ^{175}Hf, ^{183}Re and ^{184}Re were obtained from a common fit, which explains the equality of the χ^2_{pdf}'s and the attenuation thicknesses for these six radionuclides. (For the ^{184}Re 903-keV line account had to be taken of the close proximity of the strong ^{172}Lu line at 901 keV.)

6.2 Time dependences

Time dependences of erosion rates were obtained in the same way as described in Sect. 5, *viz* by integrating the two differential equations eqs. 1 and 2 in Sect. 4, and fitting to measured count rate data. For TS-2 targets, the functional form of the assumed rate of erosion was $s = s(t) = a_0 + a_1 \exp(a_2 t)$, and the three parameters a_0, a_1 and a_2, together with an initial count rate at time $t = 0$, were fitted in a four-parameter fit to the sets of measured radionuclide gamma-ray count rates for each target. The fits were made to count rate data from TS-2 targets #7, #8 and #9, since these were the only targets irradiated over extended times during which no changes[2] that could affect count rates were made in the target services area. A typical fit is shown as Fig. 9.

Since, as mentioned in Sect. 2, activity from TS-2 targets has leaked at times into the target cooling water circuit, Monte Carlo calculations were carried out of radionuclide inventories in twenty-seven regions of TS-2 targets as shown in Fig. 10. As before, the activity calculations were performed using the Monte Carlo codes MCNPX 2.70, HTAPE3X and CINDER-90. The CEM03 physics model [23] and ENDF/B-VII cross-section library [24] were used, and MCNPX was forced to use tables (if available) for neutron interactions up to the CINDER-90 upper limit of 25 MeV. The most likely regions from which activity could leak into the cooling water are regions 1, 10, 19 and 20, and, on average, for these regions, radionuclide specific activities were in the ratios of roughly 1.00 : 0.25 : 0.05 : 0.03 respectively.

[2] For example, filter changes or ion-exchange column changes.

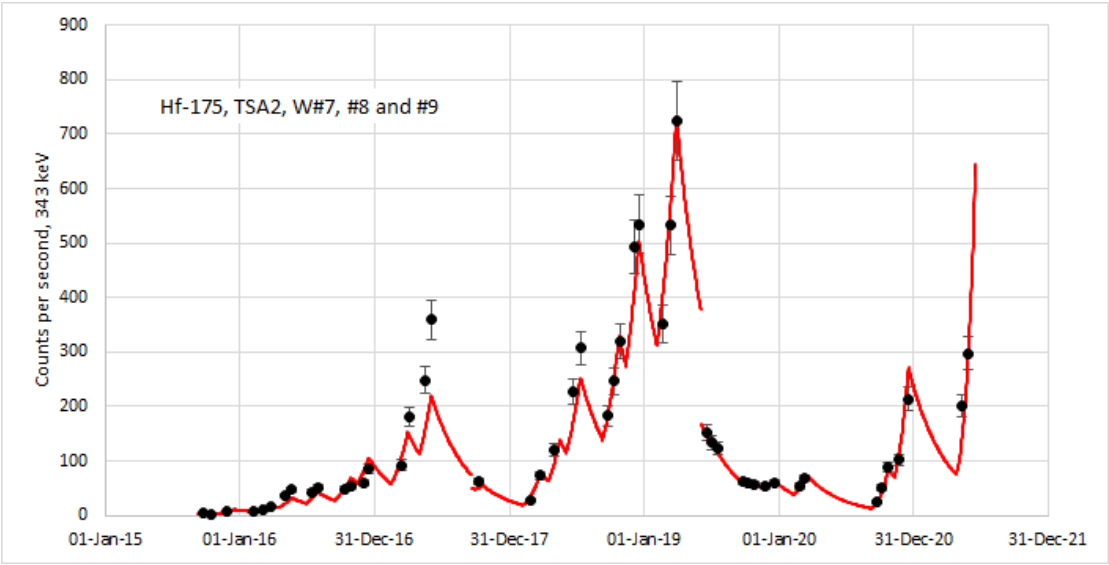

Fig. 9. Fits of erosion function $s = s(t) = a_0 + a_1 \exp(a_2 t)$ to count rate data for ^{175}Hf in forty-nine gamma-ray spectra measured in TSA2. The discontinuities in the fitted red lines occur when targets are changed.

19	20	21	22	23	24	25	26	27
10	11	12	13	14	15	16	17	18
1	2	3	4	5	6	7	8	9
10	11	12	13	14	15	16	17	18
19	20	21	22	23	24	25	26	27

Fig. 10. The twenty-seven regions into which TS-2 targets were divided and in which Monte Carlo calculations of radionuclide inventories were carried out. Schematic diagram only, not to scale. Light grey, tungsten; dark grey, tantalum; blue, cooling water. Masses in regions 1, 10, 19 and 20 are 146, 385, 212 and 990 grams respectively. There is a circumferential weld in the tantalum cladding outside the junction between regions 19 and 20.

By integrating $s(t) = a_0 + a_1 \exp(a_2 t)$ over the period of time spanned by each target so that $S = \int s(t)dt = \int \{a_0 + a_1 \exp(a_2 t)\}\, dt$, and relating count rates at 19–21 December 2020 to calculated activities within region 1 in the W#9 target at 19–21 December 2020, the absolute erosion fractions *S* listed in Table 7 were obtained. Absolute erosion fractions were obtained similarly for regions 10, 19 and 20.

Since the mass of region 1 of the target is 146 g, the absolute erosion fractions in Table 7 may be multiplied by this mass to obtain the masses of target material that have been eroded assuming that the material has been eroded from region 1, and these masses are listed in Table 8. In addition, since the cooling water is in contact with all the tantalum in the target, Table 8 also lists the mass of tantalum eroded assuming that the ^{182}Ta is eroded from the total mass 8100 g of tantalum in the target.

Similarly, from absolute erosion fractions for region 20 and the mass (990 g) of region 20, masses eroded, assuming that material is eroded from region 20, are listed in Table 9. For regions 10 and 19, estimated values of eroded masses are roughly ~300–400% of the region-1 values and ~60% of the region-20 values respectively.

Radionuclide	$S = \int\{a_0 + a_1 \exp(a_2 t)\}\, dt$		
	#7	#8	#9
^{167}Tm	5.16 ± 1.90E-03	1.27 ± 0.40E-02	3.18 ± 1.11E-02
^{169}Yb	3.87 ± 1.55E-03	9.62 ± 3.28E-03	2.11 ± 0.76E-02
^{172}Lu	3.15 ± 0.60E-03	7.33 ± 1.50E-03	8.70 ± 2.32E-03
^{172}Hf	3.51 ± 1.45E-03	1.53 ± 0.63E-02	3.88 ± 1.97E-03
^{175}Hf	6.20 ± 2.00E-03	2.06 ± 0.60E-02	1.74 ± 0.54E-02
^{182}Ta	1.02 ± 0.20E-02	1.51 ± 0.29E-02	1.68 ± 0.34E-02
^{182}Ta (all)	1.26 ± 0.24E-05	1.85 ± 0.36E-05	2.06 ± 0.42E-05
^{183}Re	0.95 ± 1.78E-03	1.72 ± 3.20E-03	1.93 ± 3.65E-03
^{184}Re	3.18 ± 1.73E-04	9.96 ± 1.97E-04	1.36 ± 0.31E-03

Table 7. Values of absolute erosion fractions for TS-2 targets #7, #8 and #9 based on activities in target region 1 (*i.e.* just behind the target nose). In addition, since the cooling water is in contact with all the tantalum in the target, the line labelled ^{182}Ta (all) corresponds to the total ^{182}Ta activity in the target and the total mass of tantalum in the target, 8100 g. For each target, the integration is over all beam-on days. Uncertainties were obtained by the 'perturbation' method described earlier.

Radionuclide	Eroded masses, grams		
	#7	#8	#9
^{167}Tm	0.75 ± 0.28	1.86 ± 0.59	4.64 ± 1.63
^{169}Yb	0.57 ± 0.23	1.41 ± 0.48	3.08 ± 1.11
^{172}Lu	0.46 ± 0.09	1.07 ± 0.22	1.27 ± 0.34
^{172}Hf	0.51 ± 0.21	2.23 ± 0.92	0.57 ± 0.29
^{175}Hf	0.91 ± 0.29	3.01 ± 0.87	2.54 ± 0.79
^{182}Ta	1.50 ± 0.29	2.20 ± 0.42	2.45 ± 0.50
^{182}Ta (all)	0.10 ± 0.02	0.15 ± 0.03	0.17 ± 0.03
^{183}Re	0.14 ± 0.26	0.25 ± 0.47	0.28 ± 0.53
^{184}Re	0.05 ± 0.02	0.15 ± 0.03	0.20 ± 0.05

Table 8. Estimated values of eroded masses of target material from TS-2 targets assuming that material (tungsten) is being eroded from region 1 of the target (just behind the nose of the target, as in Fig. 10). In addition, the line labelled ^{182}Ta (all) corresponds to the eroded mass assuming that erosion is solely from the tantalum in the target.

Radionuclide	Eroded masses, grams		
	#7	#8	#9
^{167}Tm	45 ± 17	112 ± 35	279 ± 98
^{169}Yb	13 ± 5	31 ± 11	68 ± 24
^{172}Lu	19 ± 4	45 ± 9	53 ± 14
^{172}Hf	20 ± 8	85 ± 35	21 ± 11
^{175}Hf	19 ± 6	64 ± 19	54 ± 17
^{182}Ta	31 ± 6	45 ± 19	51 ± 17
^{183}Re	5 ± 10	9 ± 18	11 ± 20
^{184}Re	2 ± 1	7 ± 1	9 ± 2

Table 9. Estimated values of eroded masses of target material from TS-2 targets assuming that the material is being eroded from region 20 of the target (at the circumferential weld around the base of the nose of the target, as in Fig. 10).

6.3 Discussion

If the data and analyses that resulted in the numbers for eroded masses in Tables 8 and 9 were perfect, then for each target the values of eroded masses obtained via the different radionuclides would be all the same. This is clearly not so, but, in view of the difficulty in establishing what the absolute activities of radionuclides in the target services area TSA2 for the TS-2 target station actually are, in view of the lack of knowledge about exactly where within the target spallation products are located relative to breaches in the cladding, in view of the inevitable uncertainties in the Monte Carlo calculations[3], and in view of the approximations made in the analyses, perhaps the agreement is as good as can reasonably be expected at this stage. Nevertheless, it would appear that erosion was probably worse for targets #8 and #9 than it was for target #7.

Since there is rough consistency between eroded masses from ^{182}Ta based on ^{182}Ta activity in the tungsten target core and the eroded masses from ^{167}Tm, ^{169}Yb, ^{172}Lu, ^{172}Hf and ^{175}Hf, whereas the eroded masses from ^{182}Ta derived on the assumption that the ^{182}Ta arises from erosion of the tantalum cladding are much smaller, it is concluded that little of the observed ^{182}Ta activity is due to erosion of the cladding. This is not inconsistent with the fact that the ^{182}Ta activity seen in the TS-1 target services area (Table 3) is only a few percent of the ^{182}Ta activity seen in the TS-2 target services area.

Since many of the masses in Table 9 are simply too large to be believable, it seems likely that erosion is taking place at or near the nose of the target rather than at the circumferential weld, *i.e.* the target would appear to be being damaged at the very place where the target is 'hit hardest' by the beam. Of course, such damage at the nose may be in addition to damage from failure of the circumferential weld about which concerns were expressed in [11].

It seems unlikely that tantalum-on-tantalum fretting leading to exposure of the tungsten core to the cooling water contributes significantly to the overall erosion process in TS-2

[3] For example, the statistical uncertainties of calculated activities are at the level of 6%, 16%, 23% and 20% for target regions 1, 10, 19 and 20, respectively. In addition, there are uncertainties in the particle-tracking procedures used in Monte Carlo computer codes, for example from uncertainties in the physical and geometrical modelling, from uncertainties in cross-section values in the nuclear data libraries used, and from the consequences of choosing particular physics model for use in the simulations. Estimated systematic uncertainties here can be at least ±20%.

targets. In these targets there are generous clearances between tantalum components everywhere except where the tantalum cross-flow guide at the front of the target (the 6-mm-thick tantalum item in Fig. 2) is joined to the tantalum cladding over the tungsten core, but here the tantalum cladding over the tungsten core is 3 mm thick — a thickness unrealistically great to be removed by fretting.

The values of eroded mases deduced via the rhenium radionuclides are noticeably smaller than the mass values deduced via the other radionuclides. It could be because rhenium is less easily leached into the ionised target cooling water than thulium, ytterbium, lutetium, hafnium and tantalum, and/or because rhenium is less easily immobilised in the TS-2 target services area (*e.g.* in the ion-exchange resins) for the gamma-ray detector to see than the other elements, and/or because of uncertain nuclear data in the Monte Carlo calculations — it is simply not known at present.

Part of the problem is that the spatial distribution of radioactivity in TSA2 cannot be measured accurately without unacceptably interrupting the operations of a heavily committed user-based facility, and so, for the readily foreseeable future, estimates of absolute activities in TSA2, and, consequently, guidance on performances of individual targets and pointers towards design changes, are likely to have to involve simplifying approximations of the sort made in the present paper.

Further work, including Monte Carlo computations of even more detailed spatial distributions of spallation products within the tungsten core, might, in principle, be worthwhile in order to improve the consistency of the mass losses for different radionuclides.

Eventually, of course, circumstances and resources may allow destructive examination of targets, whereupon results from the present proxy method may be superseded. But, for the time being, analyses of the actual performance of targets as described in the present paper represent valuable guidance for future design changes to targets.

7. Summary and conclusions

A ‘proxy’ method involving gamma-ray spectrometry has been used to extract absolute erosion rates in neutron-producing targets at the ISIS Spallation Neutron and Muon Source. Many approximations and assumptions have been made along the way (the principal assumption being that material eroded from a target ends up in the target services area where it is seen by the HPGe gamma-ray detector), but estimates for TS-1 targets are several milligrams lost over a typical ~5-years-long target lifetime, and for TS-2 targets ~1 gram lost over a typical ~2-years-long target lifetime.

During the lifetime of a TS-1 target, erosion rates appear gradually to decrease, whereas, during the lifetime of a TS-2, target erosion rates markedly increase. For TS-2 targets the time dependence of the erosion rate is not inconsistent with the view that in a fresh target it takes some time for a crack to appear in the tantalum cladding, but once the crack does appear it opens up increasingly rapidly as corrosion of the underlying tungsten proceeds.

For TS-2 targets, the most reasonable interpretation of the results is that failure of the tantalum cladding is occurring on axis at the nose of the target where the proton flux density is highest — 1.1×10^{14} protons cm^{-2} s^{-1}.

References

[1] G S Bauer, Nucl. Instr. Meth. A463 (2001) 505.

[2] https://neutrons.ornl.gov/sns

[3] https://j-parc.jp/c/en/index.html

[4] https://www.psi.ch/en/sinq

[5] http://english.ihep.cas.cn/csns/doc/1959.html

[6] https://www.isis.stfc.ac.uk/

[7] https://lansce.lanl.gov/

[8] https://europeanspallationsource.se/

[9] For example, https://neutronsources.org/calendar/regular-events/icans

[10] J W G Thomason, Nucl. Instr. Meth. A917 (2019) 61.

[11] A Dey and L G Jones, J. Nuclear Materials, 506 (2018) 63.

[12] G J Burns *et al.*, Nucl. Inst. Meth. B478 (2020) 158.

[13] D J S Findlay, B Jones and D J Adams, Nucl. Inst. Meth. A889 (2018) 113.

[14] D J S Findlay *et al.*, Appl. Radiat. Isot. 125 (2017) 1.

[15] D J S Findlay, G P Škoro and G J Burns, J. Radiol. Prot. 38 (2018) N36.

[16] D J S Findlay, Radiat. Meas. 94 (2016) 23.

[17] https://www.nist.gov/pml/x-ray-mass-attenuation-coefficients

[18] MCNPX 2.7.0 — Monte Carlo N-Particle Transport Code System for MultiParticle and High-Energy Applications, https://mcnpx.lanl.gov/

[19] W L Wilson *et al.*, Proc. SARE4 Workshop, Knoxville, USA, 1998.

[20] M-D Bermúdez *et al.*, Wear 258 (2005) 693–700.

[21] R Scott Lillard *et al.*, Los Alamos Report LA-UR-97-5011 (1997).

[22] O Caretta, T Davenne, C J Densham, J. Nucl. Materials 492 (2017) 52.

[23] S G Mashnik *et al.*, J. Phys.: Conference Series 41 (2006) 340–351. doi:10.1088/1742-6596/41/1/037.

[24] M B Chadwick *et al.*, Nucl. Data Sheets 112 (2011) 2887.